JACS
JOURNAL OF THE AMERICAN CHEMICAL SOCIETY
Article
Cite This: J. Am. Chem. Soc. 2019, 141, 6013−6021
pubs.acs.org/JACS

Controlling Nanoparticle Orientations in the Self-Assembly of Patchy Quantum Dot-Gold Heterostructural Nanocrystals

Hua Zhu,[†] Zhaochuan Fan,[‡] Long Yu,[§] Mitchell A. Wilson,[‡] Yasutaka Nagaoka,[†] Dennis Eggert,[∥,⊥] Can Cao,[†] Yuzi Liu,[#] Zichao Wei,[¶] Xudong Wang,[¶] Jie He,[¶] Jing Zhao,[¶] Ruipeng Li,[▽] Zhongwu Wang,[⊗] Michael Grünwald,*[,‡] and Ou Chen*[,†]

[†]Department of Chemistry, Brown University, Providence, Rhode Island 02912, United States
[‡]Department of Chemistry, University of Utah, Salt Lake City, Utah 84112, United States
[§]Department of Material Science and Engineering, University of Florida, Gainesville, Florida 32611, United States
[∥]Max Planck Institute for the Structure and Dynamics of Matter, Hamburg 22761, Germany
[⊥]Heinrich Petter Institute-Leibniz Institute for Experimental Virology, Hamburg 20251, Germany
[#]Center for Nanoscale Materials, Argonne National Laboratory, Argonne, Illinois 60439, United States
[¶]Department of Chemistry, University of Connecticut, Storrs, Connecticut 06269, United States
[▽]National Synchrotron Light Source II, Brookhaven National Laboratory, Upton, New York 11973, United States
[⊗]Cornell High Energy Synchrotron Source, Cornell University, Ithaca, New York 14853, United States

Supporting Information

ABSTRACT: Self-assembly of nanocrystals is a promising route for creating macroscale materials that derive function from the properties of their nanoscale building blocks. While much progress has been made assembling nanocrystals into different superlattices, controlling the relative orientations of nanocrystals in those lattices remains a challenge. Here, we combine experiments with computer simulations to study the self-assembly of patchy heterostructural nanocrystals (HNCs), consisting of near-spherical quantum dots decorated with regular arrangements of small gold satellites, into close-packed superlattices with pronounced orientational alignment of HNCs. Our simulations indicate that the orientational alignment is caused by van der Waals interactions between gold patches and is sensitive to the interparticle distance in the superlattice. We demonstrate experimentally that the degree and type of orientational alignment can be controlled by changing ligand populations on HNCs. This study provides guidance for the design and fabrication of nanocrystal superlattices with enhanced structural control.

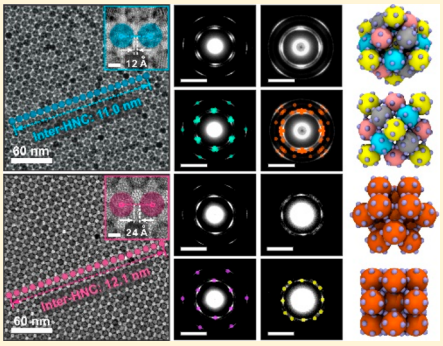

INTRODUCTION

The self-assembly of nanocrystals (NCs) with well-defined shape, size, and composition is an inexpensive and scalable method for fabricating functional nanomaterials. The properties and performance of such materials depend not only on the properties of the NC building blocks, but also on their spatial organization within the material, as characterized by nearest-neighbor distances, packing fraction, and relative orientations of NCs. Much progress has been made in the self-assembly of NCs into different superlattices (SL) and quasi-crystalline structures.[1−27] By also controlling the relative orientations of NCs within a SL, NC solids with coherent atomic lattices and extraordinary electronic properties can be fabricated.[28−37] For instance, calculations predict that two-dimensional solids of epitaxially connected quantum dots (QDs) can display a complete delocalization of charge carriers.[34] However, self-assembly of NC SLs with orientational order remains challenging in many cases because it requires anisotropic NC interactions. While NCs with distinct polyhedral shapes provide such interactions naturally,[4,38,39] many types of NC are approximately spherical, complicating the control of NC orientations.

Anisotropic NC interactions can be achieved with so-called patchy particles whose surfaces are patterned with attractively interacting regions.[2,4,7,22,40−48] On the nanoscale, patchy particles can be realized by combining two or more chemically distinct NCs in a single nanostructure. Fabrication of such heterostructural NCs (HNC), however, requires precise control over the morphology, size, and shape of multiple NC components. Owing to these challenges, pronounced orientational order or atomistic alignment of self-assembled HNCs has rarely been demonstrated to date.

Received: February 1, 2019
Published: March 19, 2019

Downloaded via BROWN UNIV on April 22, 2019 at 17:42:00 (UTC).
See https://pubs.acs.org/sharingguidelines for options on how to legitimately share published articles.

© 2019 American Chemical Society

DOI: 10.1021/jacs.9b01033
J. Am. Chem. Soc. 2019, 141, 6013−6021

Here, we report a study of quasi-spherical HNCs, comprised of QDs decorated with small Au-satellites. We demonstrate that these Au-satellites grow selectively and epitaxially on specific facets of the QD-host, resulting in an ensemble of patchy particles with regular placement of patches. Upon solvent evaporation, QD-Au HNCs assemble into a face-centered-cubic (*fcc*) SL with a large degree of atomic alignment of the hexagonal wurtzite (WZ) QD-hosts. Combining real- and reciprocal space characterization techniques, we determine the details of HNC orientations with high precision. Molecular dynamics (MD) computer simulations of a coarse-grained model of HNCs reveal that HNCs align because of attractive van der Waals (vdW) interactions between Au-satellites and that the effective strength of these interactions can be modulated by changing the surface ligand populations of HNCs, enabling the controlled assembly of SLs with different types of orientational order. This study represents an important step toward the design and fabrication of self-assembled nanomaterials with exquisite structural control extending from the macroscopic level down to the rotational state of single building blocks.

RESULTS AND DISCUSSION

Synthesis and Characterization of Patchy QD-Au Host-Satellite HNC Building Blocks. QD-Au host-satellite HNCs were synthesized using our previously published method.[49] Transmission electron microscope (TEM) images revealed a narrow size and shape distributions of both QD-hosts (9.7 ± 0.5 nm in diameter) and Au-satellites (2.2 ± 0.3 nm in diameter) (Figures 1a and S1). The host-satellite morphology of HNCs was confirmed by three-dimensional (3D) electron tomography movies (Figure 1b and Movie S1) and distributions of Cd, S, and Au atoms, as measured by high-angle annular dark-field scanning TEM (HAADF-STEM, Figures 1d, e and S2). The average number of Au-satellites per QD-host was determined to be 11.5 (inset in Figure 1b and Movie S1–S2). Elemental analysis showed that the atomic ratio between Cd and Au was ~2.59, consistent with the calculated value of 2.64 based on the HNC geometry (Figure 1c and Table S1). Wide angle X-ray scattering (WAXS) confirmed that the WZ crystal structure of the QD-hosts remained intact after Au-satellite formation (Figure 2a and Table S2). In addition, the WAXS pattern showed two clear broad features, which were assigned to $(111)_{Au}$ and $(200)_{Au}$ (Figure 2a).[49] The calculated *d*-spacings suggested a large lattice expansion of ~18% for both the $(111)_{Au}$ and $(200)_{Au}$ planes as compared to the Au bulk *d*-spacings. This large lattice expansion indicates that Au-satellites grew epitaxially at the QD surface, which is further confirmed by high-resolution TEM (HR-TEM) measurements showing atomic fringes crossing QD-Au interfaces (Figures 2c–f and S3).[49]

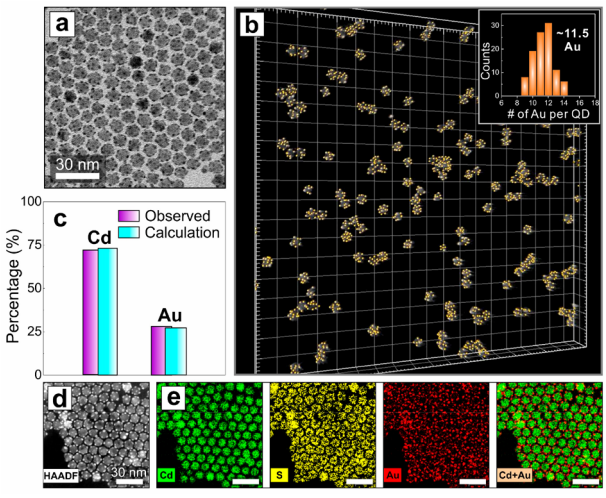

Figure 1. Characterization of QD-Au host-satellite HNC building blocks. (a) TEM image of as-synthesized QD-Au host-satellite HNCs showing high particle uniformity. (b) A snapshot from a 3D electron tomography movie (Movie S1) of QD-Au host-satellite HNCs. Inset: Histogram of the number of Au-satellites per QD-host, as obtained from electron tomography measurements. (c) Comparison of the fractions of Cd and Au atoms in HNCs from experimental data and from calculations based on the model in (b). (d) HAADF-STEM image of a monolayer of HNCs. (e) Elemental mapping (Cd, S, Au) of HNCs shown in (d).

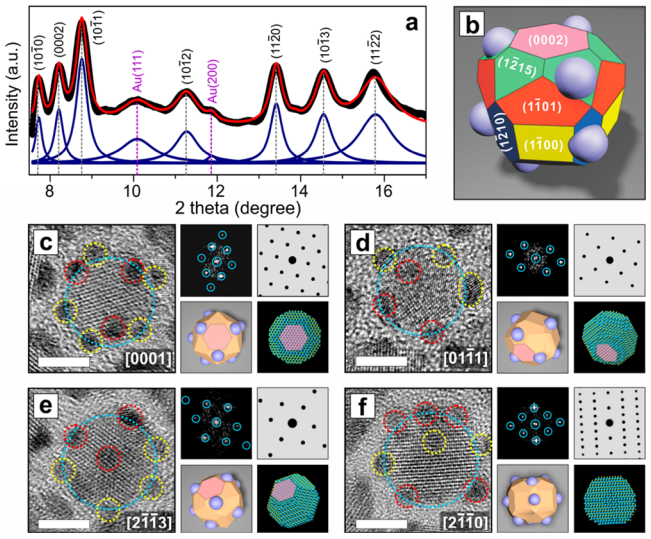

Figure 2. Characterization of Au-satellite growth at the surface of QD-hosts. (a) WAXS pattern of QD-Au host-satellite HNCs (black), fitted curve (red), and constituent peaks (blue). (b) Proposed geometric model of a typical QD-Au host-satellite HNC. (c–f) Characterization of HNC geometry from different viewing directions. Large left panels: HR-TEM images of a single HNC viewed along indicated directions. Red and yellow circles indicate Au-satellites on $\{1\bar{2}15\}_{QD}$ and $\{1\bar{1}00\}_{QD}/\{1\bar{2}10\}_{QD}$ facets, respectively. Scale bars: 5 nm. Small right panels: Fast Fourier transform (FFT) pattern of HR-TEM image (top left), computer-simulated ED pattern (top right) of atomistic QD-host model (bottom right), and geometric 3D HNC model viewed from the corresponding direction (bottom left). Light-pink color indicates the $\{0002\}_{QD}$ facets.

To characterize preferential growth sites of Au-satellites on the QD-host surface, we propose a 3D model of QD-Au HNCs based on the assumption that each QD-host is a quasi-spherical polyhedron with Au-satellites located on specific facets, as illustrated in Figure 2b. The proposed model displays five or six Au-satellites on either $\{1\bar{1}00\}_{QD}$ (yellow) or $\{1\bar{2}10\}_{QD}$ (blue) facets of the QD-host and six Au-satellites on a set of $\{1\bar{2}15\}_{QD}$ facets (green, three near the "top" and three near the "bottom" of the QD-host). In this model, Au-satellites are evenly distributed on the QD surface, a reasonable assumption given the large lattice mismatch between QD and Au and the resulting large interfacial strain.[50] The total number of 11 or 12 Au-satellites per HNC in our proposed model is consistent

DOI: 10.1021/jacs.9b01033
J. Am. Chem. Soc. 2019, 141, 6013–6021

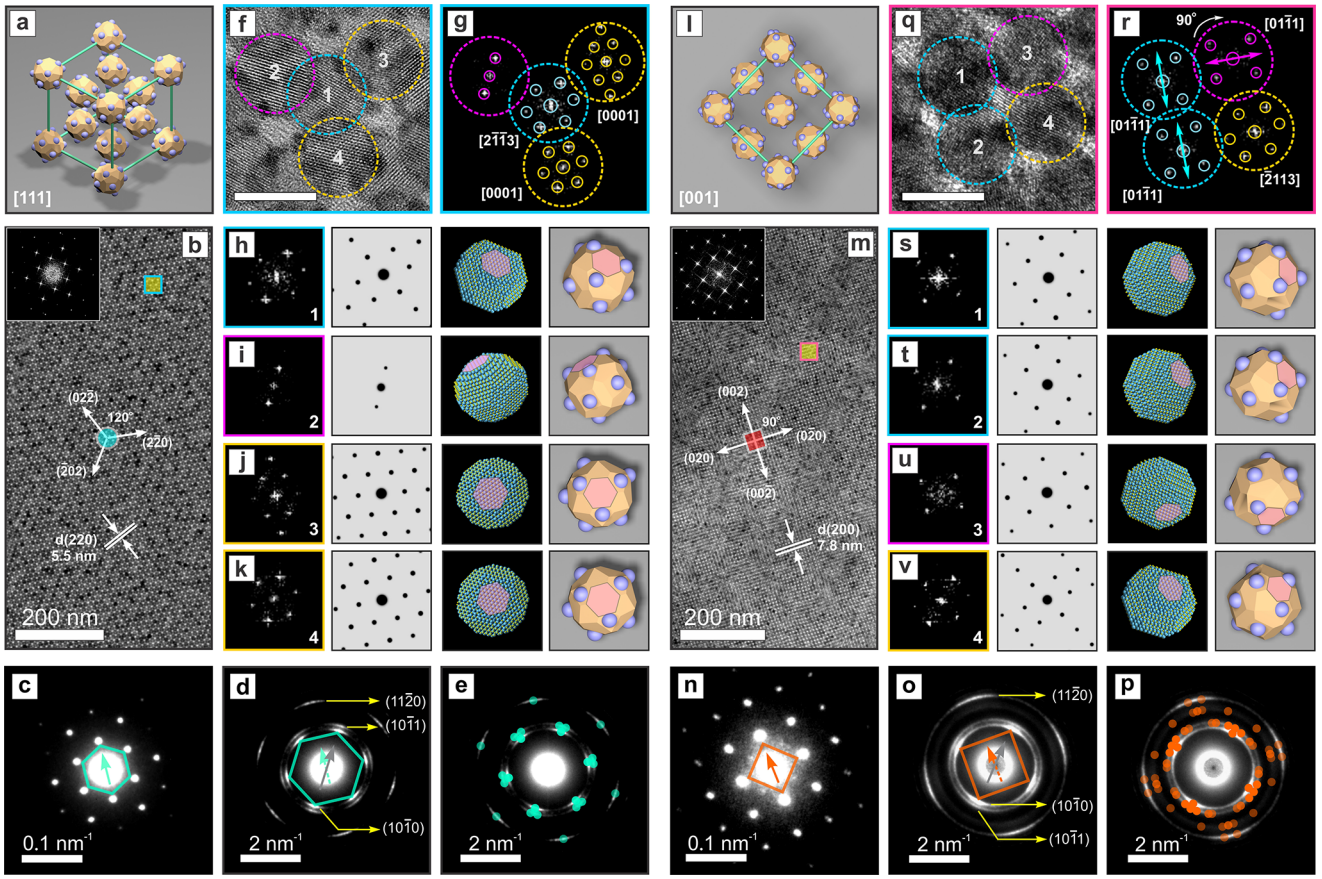

Figure 3. Atomic orientational order of HNCs inside the assembled *fcc* SL. (a) A representative 3D model of QD-Au HNC-SLs viewed along $[111]_{SL}$ zone axis. (b) A representative large area TEM image of the *fcc* HNC-SLs along $[111]_{SL}$ zone axis. Inset: corresponding FFT pattern. The corresponding SA-ED (c) and WA-ED (d) patterns and the computer-simulated WA-ED pattern (e). (f) The HR-TEM image of zoomed-in blue square area shown in (b), and (g) the corresponding FFT patterns of each individual QD-hosts. (h–k) The individual FFT patterns (left) shown in (g), computer simulated FFT patterns (middle left), computer-generated atomic models (middle right) and the corresponding 3D HNC models (right). (l) A representative 3D model of QD-Au HNC-SLs viewed along $[001]_{SL}$ zone axis. (m) A representative large area TEM image of the *fcc* HNC-SLs along $[001]_{SL}$ zone axis. Inset: the corresponding FFT pattern. The corresponding SA-ED (n) and WA-ED (o) patterns and the computer simulated WA-ED pattern (p). (q) The HR-TEM image of zoomed-in pink square area shown in (m), and (r) the corresponding FFT patterns of each individual QD-hosts. (s–v) The individual FFT patterns (left) shown in (r), computer simulated FFT patterns (middle left), computer-generated atomistic models (middle right) and the corresponding 3D HNC models (right).

with the electron tomography data (Figure 1b). Lattice interfaces observed in HR-TEM images confirmed the growth of Au-satellites on $\{1\bar{1}00\}_{QD}$ and $\{1\bar{2}10\}_{QD}$ facets (Figure S3). Due to limited spatial resolution, however, we were unable to directly observe the atomic interfaces at the $\{1\bar{2}15\}_{QD}$ facet by HR-TEM. To further confirm our proposed model, we thus compared HR-TEM images of ~100 HNCs with the proposed 3D model at different QD-host orientations. Figures 2c–f show that the Au-satellites appear in very similar positions in HR-TEM images of HNCs and in our model when viewed from several different directions (also see Figures S4–S6), suggesting that our proposed 3D model is a close approximation of the synthesized HNCs.

Characterization of Orientational Order in HNC-SLs. Upon solvent evaporation of an HNC toluene suspension (see Methods), HNCs assembled into an *fcc* SL with a lattice constant of 15.5 ± 0.3 nm, as determined by TEM (Figures 3 and S7) and small-angle X-ray scattering (SAXS, Figure S8 and Table S3). This lattice constant corresponds to a center-to-center distance of 10.9 ± 0.2 nm and an average surface-to-surface distance of 12 Å between nearest-neighbor QDs. To characterize the SL and the orientations of HNCs within the SL, we performed small- and wide-angle electron diffraction (SA/WA-ED) along $[111]_{SL}$ and $[001]_{SL}$ directions (Figure 3c,d,n,o). The obtained SA-ED patterns confirmed the SL crystallographic projections identified based on TEM images (Figure 3b,c,m,n). WA-ED patterns acquired along both SL directions displayed localized diffraction features, indicating that HNCs were not randomly oriented on their lattice sites, but showed a substantial correlation between HNC orientations (Figure 3d,o). By contrast, WA-ED patterns of SL assembled from "bare" QDs without Au-satellites showed no clear orientational ordering (Figure S9).

To identify the NC orientations that led to these WA-ED patterns, we took HR-TEM images of individual HNCs on $(111)_{SL}$ and $(001)_{SL}$ surfaces and calculated fast-Fourier transform (FFT) patterns of the observed lattice fringes (Figure 3f,g,q,r). Consistent with localized WA-ED patterns, many imaged QD-hosts displayed identical orientations. In the following discussion, we will indicate these orientations by the atomistic lattice direction that is aligned with either the $[111]_{SL}$ or $[001]_{SL}$ directions. Note that this description determines the orientational state of QDs only up to a rotation around the corresponding SL direction; for an unambiguous

DOI: 10.1021/jacs.9b01033
J. Am. Chem. Soc. 2019, 141, 6013–6021

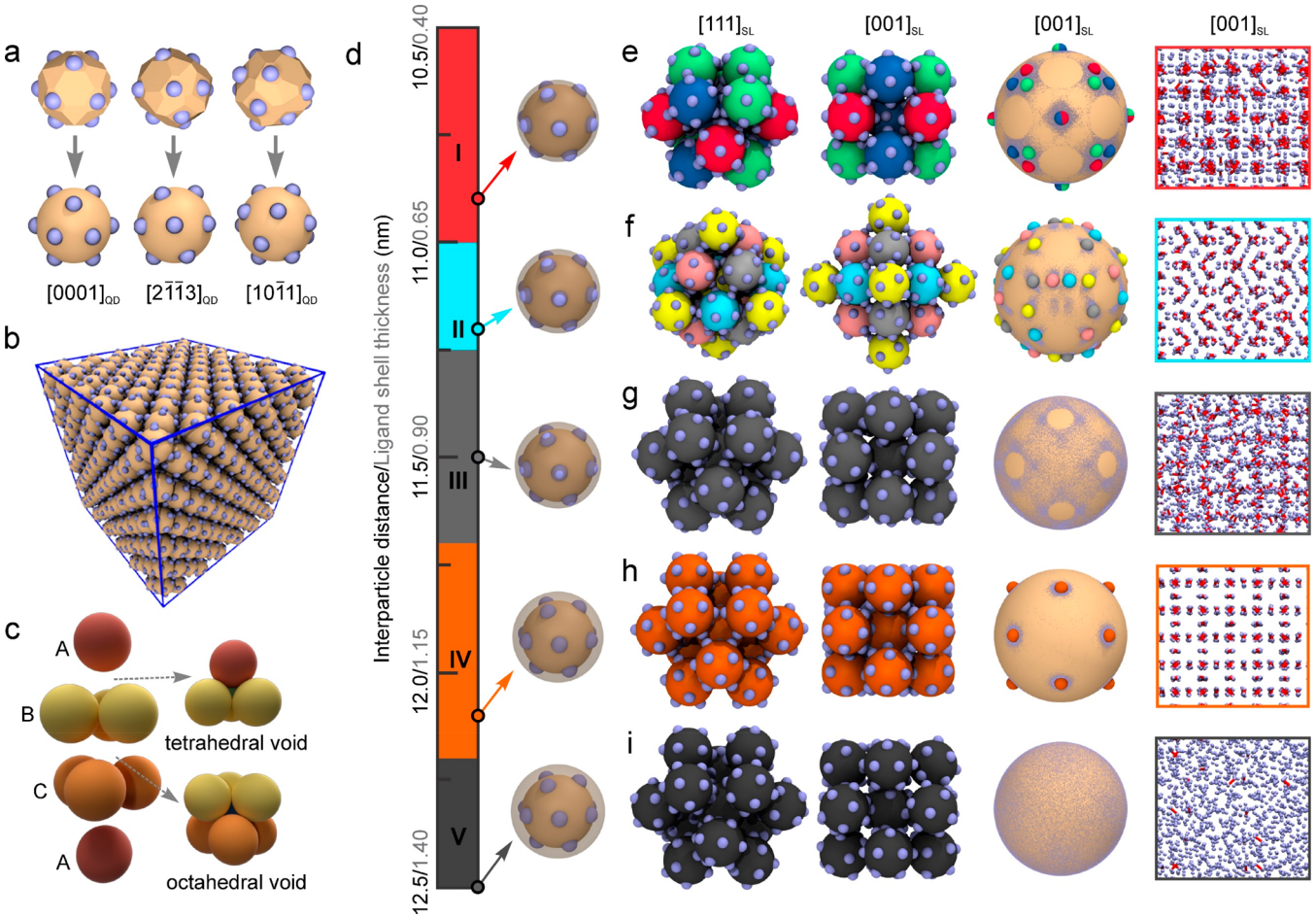

Figure 4. HNCs form SLs with different orientational order in MD simulations. (a) Comparison of satellite configurations in the polyhedral model and spherical simulation model of HNCs. (b) MD snapshot of the HNC *fcc* SL. (c) Schematic representation of the tetrahedral and octahedral voids in an *fcc* lattice with "ABCABC" stacking. (d) Illustration of five different types of orientational order (structures I–V) observed in MD simulations for different thickness of the ligand shell. For each structure, we show a snapshot of a single HNC highlighting the extent of the ligand shell (semitransparent gray). (e–i) Different orientational order in structures I–V. From left to right: close-up views of the SL in $[111]_{SL}$ and $[100]_{SL}$ projection (different colors indicate HNCs with distinct orientations, light- and dark-gray HNCs are rotationally disordered); a scatter plot of satellite positions in $[100]_{SL}$ projection (light-blue dots) from 10 ns of MD simulation (colored beads indicate average satellite positions of HNCs with distinct orientations); and a snapshot in $[100]_{SL}$ projection showing only satellites, highlighting contacts between satellites with red lines.

and complete specification of all identified QD orientations, we refer the reader to the SI.

We first discuss the orientations of HNCs we observed when the SL was viewed along the $[111]_{SL}$. In this viewing direction, we identified the QDs with lattice fringes that produce distinct 6-fold and quasi-6-fold FFT patterns, which we assigned to QDs in $[0001]_{QD}$ and $[2\bar{1}\bar{1}3]_{QD}$ orientations, respectively (Figure 3f,g). We then simulated the WA-ED patterns that arose from a WZ lattice in these particular orientations (Figure S10 and Table S4). We find that these simulated patterns agree very well with the experimental patterns, as illustrated in Figure 3h–k. Specifically, QDs in $[0001]_{QD}$ produce WA-ED signals that originate from $\{10\bar{1}0\}_{QD}$ and $\{11\bar{2}0\}_{QD}$ WZ lattice planes; QDs with $[2\bar{1}\bar{1}3]_{QD}$ orientation produce WA-ED signals originating from $\{10\bar{1}1\}_{QD}$ planes (Figure 3d). In addition to HNCs with the two orientations discussed above, many HNCs that were imaged with HR-TEM produced FFT patterns with only two discernible spots, preventing unambiguous determination of the QD orientation (e.g., particle 2 in Figure 3f,g,i). However, these particles can be accounted for by assuming that other $[111]_{SL}$ directions are equivalent to the one we analyzed and by realizing that QDs that appear in, say, $[2\bar{1}\bar{1}3]_{QD}$ orientation in one particular $[111]_{SL}$ projection will appear in a different QD orientation when the SL is viewed along different equivalent $[111]_{SL}$ directions (Figure S10–S11). Under this assumption, we enumerated all QD orientations that should be observable in any given $[111]_{SL}$ projection (given that $[0001]_{QD}$ and $[2\bar{1}\bar{1}3]_{QD}$ orientations have been identified) and simulated their respective WA-ED patterns (Figure S12 and Table S4). When plotted together, the simulated WA-ED patterns of all these QD orientations produce an excellent match with the experimental WA-ED pattern (Figure 3e).

The above analysis of QD orientations in $[111]_{SL}$ projection immediately enables us to predict a set of QD orientations that should be observable when the SL is viewed along a $[001]_{SL}$ direction. Several of these predicted orientations could indeed be directly confirmed with HR-TEM and FFT analysis of lattice fringes. In particular, we identified QDs with $[01\bar{1}1]_{QD}$ and $[\bar{2}113]_{QD}$ orientations (Figure 3q–v). QDs with these two orientations correspond to $[2\bar{1}\bar{1}3]_{QD}$-oriented QDs in $[111]_{SL}$ projection and are connected via appropriate rotations, as

DOI: 10.1021/jacs.9b01033
J. Am. Chem. Soc. 2019, 141, 6013–6021

illustrated in Figure S13. We then proceeded to simulate the WA-ED diffraction patterns for the full set of predicted QD orientations in $[001]_{SL}$ projection. The simulated patterns again agree very well with the experimental ones, as shown in Figure 2p, giving us additional confidence in our assignment of QD orientations (Figure S14−S16 and Table S5). We conclude that self-assembly of HNCs results in an *fcc* SL with well-defined relations between the orientations of WZ lattices of individual QDs that can be explained by a small set of distinct QD orientations.

In addition to orientational order of QDs, we observe an intriguing match between the symmetry of SA-ED diffraction patterns and WA-ED diffraction patterns in both viewing directions. In particular, we observe 6-fold diffraction patterns in $[111]_{SL}$ projection and 4-fold patterns in $[001]_{SL}$ projection (Figure 3c,d,n,o). Similar symmetry relations have been reported for SLs with a crystal symmetry that matches the atomistic lattice of NCs (e.g., *fcc* lattices of cubic PbS NCs).[28,29] In these cases, alignment of atomistic lattice and SL can be mediated through NC shape. In our case, however, there are no obvious relations between the cubic *fcc* SL and the atomistic WZ lattice of NCs that would explain matching SA-ED and WA-ED patterns. We hypothesize, however, that this effect is caused by the specific configuration of Au-satellites on the QD surface and their particular arrangements that form during self-assembly, which we analyze in the following section.

MD Simulations of the HNC-SL Assembly Process. To understand the driving forces responsible for the orientational alignment of HNCs observed in our experiments, we have studied the self-assembly of a simple model of HNCs with MD computer simulations. In our model, we treat QD-hosts as spherical particles with diameter of 9.7 nm. Au-satellites are represented by 12 hemispherical particles with a diameter of 2.2 nm, which are placed on the surface of QDs on positions that approximate the configuration of satellites deduced from HR-TEM images and our proposed 3D model (Figure 2b, see Methods). In our experiments, there is considerable variation in the number and configuration of Au-satellites on QD surfaces; our computational model is a reasonable approximation of a "typical" experimental HNC and agrees well with the polyhedral model, as illustrated in Figure 4a. We focus on two important interactions in our model: Interactions between oleylamine (OAm) ligands on QD surfaces and vdW attractions between Au-satellites (see Methods).[51,52] Ligands are modeled in a coarse-grained fashion, as soft spherical shells of thickness δ. Initially, we set δ = 6 Å to match the experimentally observed nearest neighbor distance of 10.9 ± 0.2 nm between HNCs in self-assembled SLs.

Simulations of the self-assembly of model HNCs resulted in *fcc* SLs, consistent with our experiments (Figures 4b and S17 and Movie S3). Our simulations furthermore suggest that attractive vdW interactions among Au-satellites are sufficiently strong to cause orientational alignment of HNCs. Specifically, HNCs adopted one of three distinct orientations in our simulations (red, green, and blue colors in Figure 4e). This particular set of HNC orientations arises because of strong interactions between Au-satellites in the tetrahedral voids (Figure 4c) of the *fcc* SL: each HNC points one satellite into each of the eight surrounding tetrahedral voids, resulting in groups of four interacting satellites in each tetrahedral void. The remaining four satellites per HNC point toward the centers of octahedral voids (Figure 4c), and do not interact strongly with other satellites. HNC orientations do not show any long-range order; in fact, we observe infrequent rotations of HNCs between these different orientations. In the following, we refer to this HNC superstructure as S−I. (Note that a similar superstructure was recently discovered for PbS NCs with polyhedral shapes).[54]

We find that the orientations of HNCs in the SL are very sensitive to changes in the interactions between HNCs. When the thickness of the ligand shell is increased from 6 to 7 Å in simulations (consistent with an increase in the HNC nearest-neighbor distance from 10.9 to 11.1 nm) we observe a strikingly different set of HNC orientations, as illustrated in Figure 4f. In this superstructure, called S−II, HNCs adopt one of four distinct orientations (as indicated by yellow, blue, pink, and gray colors in Figure 4f). Furthermore, HNC orientations in S−II display a pattern with long-range order: each HNC is surrounded by 12 HNCs with orientations that differ from its own. The abrupt change from S−I to S−II reflects different interaction patterns of Au-satellites in the two structures. Due to the larger nearest-neighbor distance, interactions of four Au-satellites in the tetrahedral voids of the *fcc* lattice are less effective. In S−II, pairs of satellites approach closely and interact strongly in the space between nearest-neighbor HNCs, resulting in stronger vdW interactions compared to S−I.

Upon further increase of the ligand shell thickness δ, HNCs undergo several additional orientational transformations. Between δ = 8 Å and δ = 10 Å, we observe HNCs with partially disordered orientations (Figure 4g). In this structure (S−III), many different HNC orientations result in comparable potential energy of satellite interactions and HNCs can rotate almost freely, as evident from the scatter plot of satellite positions in Figure 4g. (Note that HNCs do not take on certain orientations which would result in overlap of Au-satellites on nearest-neighbor HNCs.) HNCs again adopt well-defined, fixed orientations when the ligand shell thickness is further increased. Between δ = 10 Å and δ = 13 Å, we observe a superstructure (S−IV) of HNCs with uniform orientations, as illustrated in Figure 4h. Au-satellites interact directly along the lines connecting the centers of neighboring HNCs. Finally, when the ligand shell thickness is increased beyond 13 Å, vdW interactions between Au-satellites become too weak to induce orientational order and we observe a plastic *fcc* SL with entirely disordered HNC orientations (S−V, Figures 4i and S18 and Movie S4−S5).

How do HNC orientations observed in simulations compare to our experiments? Due to small experimental variations in size and shape of QD-hosts and Au-satellites, as well as variations in the number and location of satellites on individual HNCs (Figure 1), the phase behavior of HNCs in our experiments likely differs somewhat from our simulations. Nevertheless, a comparison between experiments and simulations is possible by assigning orientations to simulated HNC based on the arrangements of Au-satellites that are visible from different SL directions (see Figure 4a). The nearest-neighbor distance of HNCs measured by SAXS, 10.9 ± 0.2 nm, coincides with the phase boundary of the S−I and S−II structures in our simulations. In fact, there are striking similarities between QD orientations in experiments and in the S−II superstructure found in simulations. Both QD orientations that could be unambiguously identified by HR-TEM in $[111]_{SL}$ projection (i.e., HNCs with $[0001]_{QD}$ and $[2\bar{1}\bar{1}3]_{QD}$ alignments) can also be assigned in simulation snapshots of the S−II: pink QDs in S−II have $[0001]_{QD}$ alignment, while yellow, blue and gray QDs are consistent with

DOI: 10.1021/jacs.9b01033
J. Am. Chem. Soc. 2019, 141, 6013−6021

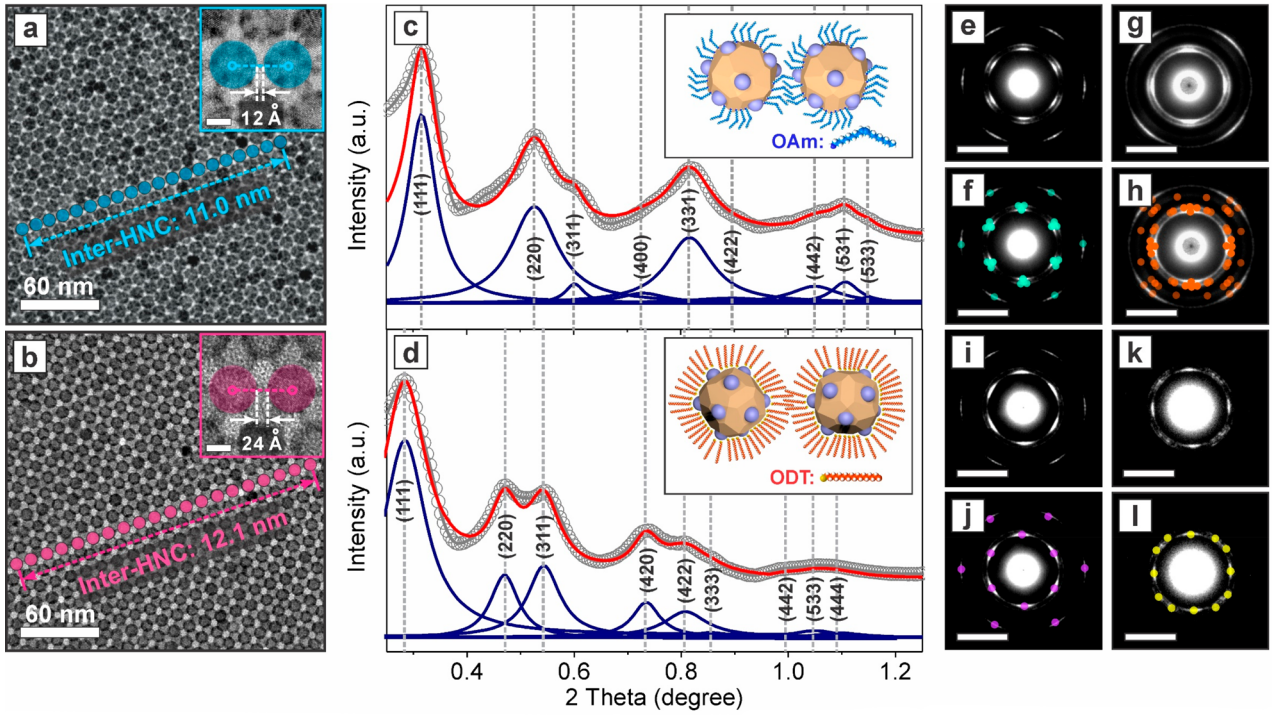

Figure 5. Control of HNC orientations via ligand layer thickness. (a,b) TEM images of the HNC-SL viewed along the close-packed $[111]_{SL}$ zone axis, assembled from OAm (a) and ODT (b) passivated HNCs with different surface ligand density. Insets: zoomed-in TEM images of the HNC-SL. Scale bars: 5 nm. (c,d) SAXS patterns of the corresponding HNC-SLs. (e–l) Experimental (e,g,i,k) and computer-simulated (f,h,j,l) WA-ED patterns along $[111]_{SL}$ (e,f,i,j) and $[001]_{SL}$ (g,h,k,l) for the HNC-SL assembled from OAm (e–h) and ODT (i–l) passivated HNCs. Scale bars: 2 nm^{-1}.

$[2\bar{1}\bar{1}3]_{QD}$ alignment (Figures 3f,g, and 4f, and S19). In $[001]_{SL}$ projection, S–II also displays QD orientations that correspond well to the $[01\bar{1}1]_{QD}$ and $[\bar{2}113]_{QD}$ alignment found experimentally (Figures 3q,r, 4f, and S18), indicating that the experimental SL is closely related to the S–II superstructure found in simulations.

Controlling Orientational Order. Most intriguingly, our computer simulations suggest a means of tuning the orientational alignment of HNCs, by changing the thickness of ligand layers on HNCs. To validate this prediction, we have performed additional self-assembly experiments with 1-octadecanethiol (ODT) covered HNCs, as obtained by postsynthetic ligand exchange (see SI). Fourier-transform infrared spectroscopy showed that no OAm ligands remained on HNCs after ligand exchange (Figure S20). Thermogravimetric analysis demonstrated that the surface density of ligands increased from ~3 ligands/nm^2 to ~9 ligands/nm^2, consistent with the strong binding affinity of thiols to both the Au and QD surfaces (Figure S21).[55] ODT-passivated HNCs were assembled into well-ordered *fcc* SLs with a markedly increased lattice constant of 17.1 nm and a corresponding nearest-neighbor distance of 12.1 nm (Figures 5a–d and S22–S23 and Table S6). This substantial lattice expansion is consistent with an increase of the ligand shell thickness from 6 to 12 Å and is clearly visible in TEM images (Figure 5a,b). In simulations, these ligand shell thicknesses result in strikingly different superstructures, i.e., S–I and S–IV, respectively. In S–IV, all QD-hosts have the same orientation, consistent with $[0001]_{QD}$ alignment. An analogous change of atomistic alignment is in fact observed in our experiments, as evident from a comparison of WA-ED patterns of the HNC-SL obtained with the two different types of ligands (Figure 5e–l): While strong signals from HNCs in $[0001]_{QD}$ alignment can be seen in both WA-ED patterns, $\{10\bar{1}1\}_{QD}$ signals originated from HNCs in $[2\bar{1}\bar{1}3]_{QD}$ alignment are absent for ODT-passivated HNCs, indicating a decrease of $[2\bar{1}\bar{1}3]_{QD}$ in favor of $[0001]_{QD}$ alignment. WA-ED patterns obtained in $[001]_{SL}$ projection further confirm a marked change in orientational order of HNCs (Figures 5k,l and S24–S26). Our experiments and simulations thus demonstrate that appropriate choices of ligands can be used to control the degree of orientational order of HNCs inside the SLs.

CONCLUSION

This paper describes a new route to independently control the translational and orientational order of self-assembled NCs. The strategy we present relies on the synthesis of HNCs that act as patchy particles. A highly regular, if not completely uniform, placement of patches is crucial, and is achieved here by exploiting the preferential growth of Au-satellites on particular facets of quasi-spherical QD-hosts. This synthetic strategy can likely be extended to other materials. In addition to the epitaxial growth of satellites demonstrated here, other possible routes to achieve patchy nanoparticles include the use of facet-specific surface chemistry and hierarchical self-assembly strategies.[2,4,56] Our work furthermore highlights the still underappreciated role of ligands in determining nanoparticle interactions and assembly outcomes. We anticipate that advances in both the synthesis of HNCs as well as control of surface chemistry of NCs will enable self-assembly of complex NC superstructures with exquisite structural control from the atomistic up to the macroscopic level.

DOI: 10.1021/jacs.9b01033
J. Am. Chem. Soc. 2019, 141, 6013–6021

METHODS

Synthesis of CdSe-CdS Core−Shell QDs. CdSe-CdS core−shell QDs were synthesized using a previously published method with minor modification.[57]

Synthesis of CdSe core: briefly, 60 mg CdO, 280 mg octadecylphosphonic acid (ODPA) and 3.0 g trioctylphosphine oxide (TOPO) were added to a 50 mL flask. The mixture was heated to 150 °C and degassed under vacuum for 1 h. Under nitrogen flow, the reaction mixture was further heated to 320 °C to form a colorless clear solution. After adding 2.0 mL trioctylphosphine (TOP) to the solution, the temperature was quickly heated up to 380 °C, at which point Se/TOP (60 mg Se in 0.5 mL TOP) solution was injected quickly into the flask. When the CdSe core QDs reached the desired size, the reaction was terminated by removing the heat. After cooling down to room temperature, the resulting CdSe QDs were precipitated by adding acetone and redispersed in hexane for further uses.

CdS shell growth: a hexane solution containing 200 nmol of CdSe core QDs was loaded in a mixture of 4.0 mL 1-octadecene (ODE) and 4.0 mL oleylamine (OAm). The reaction solution was degassed under vacuum at room temperature for 1 h and 120 °C for another 20 min to completely remove the hexane, water and oxygen inside the reaction solution. After that the reaction solution was heated up to 240 °C at which point a desired amount of cadmium(II) oleate (6 monolayers (MLs), diluted in 4.0 mL ODE) and 1.2 equiv amount of ODT (diluted in 4.0 mL ODE) were injected into the growth solution at a rate of 2 ML/h using a syringe pump. Meanwhile, the reaction temperature was further raised to 310 °C and maintained for the rest of the reaction. During the growth, 1.0 mL oleic acid was injected every hour. After finishing the precursor infusion, another 1.0 mL oleic acid was quickly injected and the solution was further annealed at 310 °C for 30 min. The resulting CdSe-CdS core−shell QDs were precipitated by adding acetone, and then redispersed in toluene as a stock solution.

Synthesis of QD-Au Host-Satellite HNCs. QD-Au host-satellite HNCs were synthesized using previous published method with modification.[58] Typically, 3.0 mg as synthesized CdSe-CdS core−shell QDs were dispersed in 10 mL toluene and the resulting solution was heated up to 40 °C and maintained for the entire reaction. Gold precursor stock solution was prepared by adding 30 mg $AuCl_3$, 154 mg dodecyltrimethylammonium bromide (DTAB) and 0.5 mL OAm into 7.0 mL toluene and sonicated for 15 min. The solution turned to light yellow eventually. 4.0 mL of gold precursor was first filtered using 25 mm syringe filter with 0.2 μm PTFE membrane and then injected into QDs toluene solution and stirred for 1 h. The resulting QD-Au HNCs were precipitated by adding a mixture of ethanol and methanol and then redispersed in toluene. After the Au satellites growth, the emission of the QD is totally quenched.

Formation of HNC-SLs. Resulting QD-Au HNCs were dispersed in toluene and diluted to ∼2.0 mg/mL. A TEM grid was first placed on a clean silicon substrate, then ∼50 μL toluene solution was dropped on the TEM grid. The sample was further covered with a glass Petri-dish to ensure a slow solvent evaporation.

Ligand Exchange of QD-Au HNCs. The ligand exchange of QD-Au HNCs were performed by first thoroughly mixing HNCs toluene suspension (∼4.0 mg/mL) with ODT toluene solution (∼6.0 mg/mL) and then stored and remained undisturbed for ∼2 h. Finally, the resulting mixture were purified once with ethanol and methanol and then redispersed in toluene before further characterization.

TEM and ED Measurements of the QD-Au HNCs and HNC-SLs. TEM characterizations were performed on a JEOL 2100F operated at 200 kV. For the HNC building blocks, the sample in a toluene solution (∼10 μL) was dropped onto a 300-mesh copper TEM grid and dried at ambient condition. For the SA- and WA-ED measurements, we used a selected-area aperture with a diameter of ca. 0.8 μm.

STEM Measurements of the QD-Au HNCs. High-angle annular dark field (HAADF) STEM and STEM-energy dispersive X-ray spectroscopy (EDS) mapping was performed on a FEI Talos F200X. TEM/STEM is running at 200 kV equipped with SuperX EDS detector.

Electron Tomography. Tilt series were acquired in 1-degree increments from −60 to +60 degrees on a transmission electron microscope (Tecnai G2, FEI company, Eindhoven, The Netherlands) operated in bright field mode using an acceleration voltage of 200 kV. Images were recorded using bottom mounted 4K CCD camera (Eagle 4K, FEI company)

The Inspect 3D Xpress software package (v. 3.0.0.3478, FEI company) was used for image alignment and reconstruction of 3D data sets from the tilt series. The reconstructions were performed using the sequential iterative reconstruction techniques (SIRT) algorithm with 20 iterations computed on a graphics processing unit (QUADRO 5000, NVIDIA Corporation, Santa Clara, CA, USA).

Analyses Software. The *OriginPro 8.0* was used for the peak analyses such as peak fittings and determinations of peak positions. *CrystalMaker* version 9.2 and *CrystalDiffract* with version 6.6 (CrystalMaker Software Limited) were used for the WA-ED simulations.

Molecular Dynamics Simulations. In our HNC model, Au satellites are placed on the surface of QDs in the following manner: We first position the center of the QD on a lattice site of an *fcc* lattice that has a nearest-neighbor distance of 4.85 nm, equal to the radius of the QD. Au-satellites are then placed on the 12 nearest-neighbor lattice sites, as illustrated in Figure 4a of the main manuscript. Au−Au, QD−QD, and Au−QD interaction were modeled with an "expanded" Lennard-Jones potential,

$$u = 4\varepsilon\left[\left(\frac{\sigma}{r-\Delta}\right)^{12} - \left(\frac{\sigma}{r-\Delta}\right)^{6}\right] \quad (1)$$

All interaction parameters are provided in Table S7 and are discussed further in the SI. HNCs (each consisting of one QD and 12 Au-satellites) were treated as rigid bodies in simulations. The system temperature and pressure were kept at 300 K and 0 atm and were controlled by a Langevin thermostat and a Nose-Hoover barostat, respectively, as implemented in LAMMPS.[53] A time step of 10 fs was used. To construct an initial configuration of the HNC system, 864 QD-Au HNCs were placed on an *fcc* lattice consisting of 6 × 6 × 6 conventional *fcc* unit cells with a lattice parameter of 20 nm in a periodically replicated cubic simulation box. Δ_{QD} was increased in increments of 0.05 nm, and MD simulations were performed for 10 ns at each value of Δ_{QD}. An input script for LAMMPS is available as part of the SI. Orientational scatter plots (as shown in Figure 4e−i and Figure S18) were calculated by plotting the projections of all Au satellite positions (gray dots) onto the surface of a sphere centered on HNCs (yellow) over the course of 5 ns of MD simulation.

ASSOCIATED CONTENT

Supporting Information

The Supporting Information is available free of charge on the ACS Publications website at DOI: 10.1021/jacs.9b01033.

Experimental and simulation methods, additional figures, additional characterization of QD-Au HNCs and corresponding SLs, movies including electron tomography, and simulation of SL self-assembly (PDF)

Movie S1 (MOV)

Movie S2 (MOV)

Movie S3 (MOV)

Movie S4 (MOV)

Movie S5 (MOV)

Additional data (TXT)

AUTHOR INFORMATION

Corresponding Authors

*michael.gruenwald@utah.edu

*ouchen@brown.edu

DOI: 10.1021/jacs.9b01033
J. Am. Chem. Soc. 2019, 141, 6013−6021

ORCID

Hua Zhu: 0000-0003-2733-7837
Zhaochuan Fan: 0000-0001-9492-5722
Zichao Wei: 0000-0001-5818-5077
Xudong Wang: 0000-0002-1189-8181
Jie He: 0000-0003-0252-3094
Jing Zhao: 0000-0002-6882-2196
Zhongwu Wang: 0000-0001-9742-5213
Michael Grünwald: 0000-0003-2186-1662
Ou Chen: 0000-0003-0551-090X

Notes

The authors declare no competing financial interest.

■ ACKNOWLEDGMENTS

O. C. acknowledges support from the National Science Foundation (OIA-1538893) and the Brown University Startup fund. The support and resources of the Center for High Performance Computing at the University of Utah are gratefully acknowledged. This work was performed, in part, at the Center for Nanoscale Materials, a U.S. Department of Energy Office of Science User Facility, and supported by the U.S. Department of Energy, Office of Science, under Contract No. DE-AC02-06CH11357. Z. F. and M. G. acknowledge support by the National Science Foundation under Grant No. DMR-1848499. CHESS is supported by National Science Foundataion award under DMR-1332208.

■ REFERENCES

(1) Boles, M. A.; Engel, M.; Talapin, D. V. Self-Assembly of Colloidal Nanocrystals: From Intricate Structures to Functional Materials. *Chem. Rev.* **2016**, *116* (18), 11220−11289.

(2) Nagaoka, Y.; Zhu, H.; Eggert, D.; Chen, O. Single-Component Quasicrystalline Nanocrystal Superlattices through Flexible Polygon Tiling Rule. *Science* **2018**, *362* (6421), 1396−1400.

(3) Bishop, K. J. M.; Wilmer, C. E.; Soh, S.; Grzybowski, B. A. Nanoscale Forces and Their Uses in Self-Assembly. *Small* **2009**, *5* (14), 1600−1630.

(4) Nagaoka, Y.; Tan, R.; Li, R.; Zhu, H.; Eggert, D.; Wu, Y. A.; Liu, Y.; Wang, Z.; Chen, O. Superstructures Generated from Truncated Tetrahedral Quantum Dots. *Nature* **2018**, *561* (7723), 378−382.

(5) Murray, C. B.; Kagan, C. R.; Bawendi, M. G. Self-Organization of CdSe Nanocrystallites into 3-Dimensional Quantum-Dot Superlattices. *Science* **1995**, *270* (5240), 1335−1338.

(6) Tan, R.; Zhu, H.; Cao, C.; Chen, O. Multi-Component Superstructures Self-Assembled from Nanocrystal Building Blocks. *Nanoscale* **2016**, *8* (19), 9944−9961.

(7) Nykypanchuk, D.; Maye, M. M.; van der Lelie, D.; Gang, O. DNA-Guided Crystallization of Colloidal Nanoparticles. *Nature* **2008**, *451* (7178), 549−552.

(8) Lin, H. X.; Lee, S. M.; Sun, L.; Spellings, M.; Engel, M.; Glotzer, S. C.; Mirkin, C. A. Clathrate Colloidal Crystals. *Science* **2017**, *355* (6328), 931−935.

(9) Tang, Z. Y.; Kotov, N. A.; Giersig, M. Spontaneous Organization of Single CdTe Nanoparticles into Luminescent Nanowires. *Science* **2002**, *297* (5579), 237−240.

(10) Wang, T.; Zhuang, J. Q.; Lynch, J.; Chen, O.; Wang, Z. L.; Wang, X. R.; LaMontagne, D.; Wu, H. M.; Wang, Z. W.; Cao, Y. C. Self-Assembled Colloidal Superparticles from Nanorods. *Science* **2012**, *338* (6105), 358−363.

(11) Wu, L. H.; Willis, J. J.; McKay, I. S.; Diroll, B. T.; Qin, J.; Cargnello, M.; Tassone, C. J. High-Temperature Crystallization of Nanocrystals into Three-Dimensional Superlattices. *Nature* **2017**, *548* (7666), 197−201.

(12) Zhu, H.; Fan, Z.; Yuan, Y.; Wilson, M. A.; Hills-Kimball, K.; Wei, Z.; He, J.; Li, R.; Gruenwald, M.; Chen, O. Self-Assembly of Quantum Dot-Gold Heterodimer Nanocrystals with Orientational Order. *Nano Lett.* **2018**, *18* (8), 5049−5056.

(13) Raino, G.; Becker, M. A.; Bodnarchuk, M. I.; Mahrt, R. F.; Kovalenko, M. V.; Stoferle, T. Superfluorescence from Lead Halide Perovskite Quantum Dot Superlattices. *Nature* **2018**, *563* (7733), 671−675.

(14) Pileni, M. P. Self-Assembly of Inorganic Nanocrystals: Fabrication and Collective Intrinsic Properties. *Acc. Chem. Res.* **2007**, *40* (8), 685−693.

(15) Talapin, D. V.; Shevchenko, E. V.; Bodnarchuk, M. I.; Ye, X. C.; Chen, J.; Murray, C. B. Quasicrystalline Order in Self-Assembled Binary Nanoparticle Superlattices. *Nature* **2009**, *461* (7266), 964−967.

(16) Liu, Y. Z.; Lin, X. M.; Sun, Y. G.; Rajh, T. In Situ Visualization of Self-Assembly of Charged Gold Nanoparticles. *J. Am. Chem. Soc.* **2013**, *135* (10), 3764−3767.

(17) Tang, Z. Y.; Kotov, N. A. One-Dimensional Assemblies of Nanoparticles: Preparation, Properties, and Promise. *Adv. Mater.* **2005**, *17* (8), 951−962.

(18) Xia, Y. N.; Yang, P. D.; Sun, Y. G.; Wu, Y. Y.; Mayers, B.; Gates, B.; Yin, Y. D.; Kim, F.; Yan, Y. Q. One-Dimensional Nanostructures: Synthesis, Characterization, and Applications. *Adv. Mater.* **2003**, *15* (5), 353−389.

(19) Quan, Z. W.; Xu, H. W.; Wang, C. Y.; Wen, X. D.; Wang, Y. X.; Zhu, J. L.; Li, R. P.; Sheehan, C. J.; Wang, Z. W.; Smilgies, D. M.; Luo, Z. P.; Fang, J. Y. Solvent-Mediated Self-Assembly of Nanocube Superlattices. *J. Am. Chem. Soc.* **2014**, *136* (4), 1352−1359.

(20) Smith, D. K.; Goodfellow, B.; Smilgies, D. M.; Korgel, B. A. Self-Assembled Simple Hexagonal AB(2) Binary Nanocrystal Superlattices: Sem, Gisaxs, and Defects. *J. Am. Chem. Soc.* **2009**, *131* (9), 3281−3290.

(21) Ji, L.; Guo, G. N.; Sheng, H. Y.; Qin, S. L.; Wang, B. W.; Han, D. D.; Li, T. T.; Yang, D.; Dong, A. G. Free-Standing, Ordered Mesoporous Few-Layer Graphene Framework Films Derived from Nanocrystal Superlattices Self-Assembled at the Solid- or Liquid-Air Interface. *Chem. Mater.* **2016**, *28* (11), 3823−3830.

(22) Kostiainen, M. A.; Hiekkataipale, P.; Laiho, A.; Lemieux, V.; Seitsonen, J.; Ruokolainen, J.; Ceci, P. Electrostatic Assembly of Binary Nanoparticle Superlattices Using Protein Cages. *Nat. Nanotechnol.* **2013**, *8* (1), 52−6.

(23) Demirors, A. F.; Stiefelhagen, J. C. P.; Vissers, T.; Smallenburg, F.; Dijkstra, M.; Imhof, A.; van Blaaderen, A. Long-Ranged Oppositely Charged Interactions for Designing New Types of Colloidal Clusters. *Phys. Rev. X* **2015**, DOI: 10.1103/PhysRevX.5.021012.

(24) Bharti, B.; Findenegg, G. H.; Velev, O. D. Co-Assembly of Oppositely Charged Particles into Linear Clusters and Chains of Controllable Length. *Sci. Rep.* **2012**, DOI: 10.1038/srep01004.

(25) Go, D.; Kodger, T. E.; Sprakel, J.; Kuehne, A. J. C. Programmable Co-Assembly of Oppositely Charged Microgels. *Soft Matter* **2014**, *10* (40), 8060−8065.

(26) Kalsin, A. M.; Fialkowski, M.; Paszewski, M.; Smoukov, S. K.; Bishop, K. J.; Grzybowski, B. A. Electrostatic Self-Assembly of Binary Nanoparticle Crystals with a Diamond-Like Lattice. *Science* **2006**, *312* (5772), 420−4.

(27) Sun, Y. G. Interfaced Heterogeneous Nanodimers. *Natl. Sci. Rev.* **2015**, *2* (3), 329−348.

(28) Li, R. P.; Bian, K. F.; Hanrath, T.; Bassett, W. A.; Wang, Z. W. Decoding the Superlattice and Interface Structure of Truncate Pbs Nanocrystal-Assembled Supercrystal and Associated Interaction Forces. *J. Am. Chem. Soc.* **2014**, *136* (34), 12047−12055.

(29) Weidman, M. C.; Smilgies, D. M.; Tisdale, W. A. Kinetics of the Self-Assembly of Nanocrystal Superlattices Measured by Real-Time in Situ X-Ray Scattering. *Nat. Mater.* **2016**, *15* (7), 775−781.

(30) Boneschanscher, M. P.; Evers, W. H.; Geuchies, J. J.; Altantzis, T.; Goris, B.; Rabouw, F. T.; van Rossum, S. A.; van der Zant, H. S.; Siebbeles, L. D.; Van Tendeloo, G.; Swart, I.; Hilhorst, J.; Petukhov, A. V.; Bals, S.; Vanmaekelbergh, D. Long-Range Orientation and

DOI: 10.1021/jacs.9b01033
J. Am. Chem. Soc. 2019, 141, 6013−6021

Atomic Attachment of Nanocrystals in 2D Honeycomb Superlattices. *Science* **2014**, *344* (6190), 1377−80.
(31) Yang, J.; Elim, H. I.; Zhang, Q.; Lee, J. Y.; Ji, W. Rational Synthesis, Self-Assembly, and Optical Properties of PbS-Au Heterogeneous Nanostructures Via Preferential Deposition. *J. Am. Chem. Soc.* **2006**, *128* (36), 11921−6.
(32) Bian, K. F.; Choi, J. J.; Kaushik, A.; Clancy, P.; Smilgies, D. M.; Hanrath, T. Shape-Anisotropy Driven Symmetry Transformations in Nanocrystal Superlattice Polymorphs. *ACS Nano* **2011**, *5* (4), 2815−2823.
(33) van der Stam, W.; Rabouw, F. T.; Vonk, S. J. W.; Geuchies, J. J.; Ligthart, H.; Petukhov, A. V.; Donega, C. D. Oleic Acid-Induced Atomic Alignment of ZnS Polyhedral Nanocrystals. *Nano Lett.* **2016**, *16* (4), 2608−2614.
(34) Whitham, K.; Yang, J.; Savitzky, B. H.; Kourkoutis, L. F.; Wise, F.; Hanrath, T. Charge Transport and Localization in Atomically Coherent Quantum Dot Solids. *Nat. Mater.* **2016**, *15* (5), 557−563.
(35) Evers, W. H.; Goris, B.; Bals, S.; Casavola, M.; de Graaf, J.; van Roij, R.; Dijkstra, M.; Vanmaekelbergh, D. Low-Dimensional Semiconductor Superlattices Formed by Geometric Control over Nanocrystal Attachment. *Nano Lett.* **2013**, *13* (6), 2317−2323.
(36) Sandeep, C. S. S.; Azpiroz, J. M.; Evers, W. H.; Boehme, S. C.; Moreels, I.; Kinge, S.; Siebbeles, L. D. A.; Infante, I.; Houtepen, A. J. Epitaxially Connected PbSe Quantum-Dot Films: Controlled Neck Formation and Optoelectronic Properties. *ACS Nano* **2014**, *8* (11), 11499−11511.
(37) Kagan, C. R.; Murray, C. B. Charge Transport in Strongly Coupled Quantum Dot Solids. *Nat. Nanotechnol.* **2015**, *10* (12), 1013−1026.
(38) Damasceno, P. F.; Engel, M.; Glotzer, S. C. Predictive Self-Assembly of Polyhedra into Complex Structures. *Science* **2012**, *337* (6093), 453−457.
(39) Agarwal, U.; Escobedo, F. A. Mesophase Behaviour of Polyhedral Particles. *Nat. Mater.* **2011**, *10* (3), 230−235.
(40) Pawar, A. B.; Kretzschmar, I. Fabrication, Assembly, and Application of Patchy Particles. *Macromol. Rapid Commun.* **2010**, *31* (2), 150−168.
(41) Zhang, Z. L.; Glotzer, S. C. Self-Assembly of Patchy Particles. *Nano Lett.* **2004**, *4* (8), 1407−1413.
(42) Zheng, X. L.; Liu, M. Z.; He, M. X.; Pine, D. J.; Weck, M. Shape-Shifting Patchy Particles. *Angew. Chem., Int. Ed.* **2017**, *56* (20), 5507−5511.
(43) Park, S. Y.; Lytton-Jean, A. K.; Lee, B.; Weigand, S.; Schatz, G. C.; Mirkin, C. A. DNA-Programmable Nanoparticle Crystallization. *Nature* **2008**, *451* (7178), 553−556.
(44) Zhang, J. Y.; Santos, P. J.; Gabrys, P. A.; Lee, S.; Liu, C.; Macfarlane, R. J. Self-Assembling Nanocomposite Tectons. *J. Am. Chem. Soc.* **2016**, *138* (50), 16228−16231.
(45) Chen, Q.; Bae, S. C.; Granick, S. Directed Self-Assembly of a Colloidal Kagome Lattice. *Nature* **2011**, *469* (7330), 381−384.
(46) Wang, Y. F.; Wang, Y.; Breed, D. R.; Manoharan, V. N.; Feng, L.; Hollingsworth, A. D.; Weck, M.; Pine, D. J. Colloids with Valence and Specific Directional Bonding. *Nature* **2012**, *491* (7422), 51−61.
(47) Sciortino, F.; Bianchi, E.; Douglas, J. F.; Tartaglia, P. Self-Assembly of Patchy Particles into Polymer Chains: A Parameter-Free Comparison between Wertheim Theory and Monte Carlo Simulation. *J. Chem. Phys.* **2007**, *126* (19), 194903.
(48) Bianchi, E.; Largo, J.; Tartaglia, P.; Zaccarelli, E.; Sciortino, F. Phase Diagram of Patchy Colloids: Towards Empty Liquids. *Phys. Rev. Lett.* **2006**, *97* (16), 168301.
(49) Zhu, H.; Nagaoka, Y.; Hills-Kimball, K.; Tan, R.; Yu, L.; Fang, Y.; Wang, K.; Li, R.; Wang, Z.; Chen, O. Pressure-Enabled Synthesis of Hetero-Dimers and Hetero-Rods through Intraparticle Coalescence and Interparticle Fusion of Quantum-Dot-Au Satellite Nanocrystals. *J. Am. Chem. Soc.* **2017**, *139* (25), 8408−8411.
(50) McDaniel, H.; Shim, M. Size and Growth Rate Dependent Structural Diversification of Fe_3O_4/CdS Anisotropic Nanocrystal Heterostructures. *ACS Nano* **2009**, *3* (2), 434−440.
(51) Israelachvili, J. N. *Intermolecular and Surface Forces*, 3rd ed.; Academic Press: Burlington, MA, 2010.
(52) Kister, T.; Monego, D.; Mulvaney, P.; Widmer-Cooper, A.; Kraus, T. Colloidal Stability of Apolar Nanoparticles: The Role of Particle Size and Ligand Shell Structure. *ACS Nano* **2018**, *12* (6), 5969−5977.
(53) Plimpton, S. Fast Parallel Algorithms for Short-Range Molecular-Dynamics. *J. Comput. Phys.* **1995**, *117* (1), 1−19.
(54) Fan, Z.; Gruenwald, M. Orientational Order in Self-Assembled Nanocrystal Superlattices. *J. Am. Chem. Soc.* **2019**, *141* (5), 1980−1988.
(55) Pensa, E.; Cortes, E.; Corthey, G.; Carro, P.; Vericat, C.; Fonticelli, M. H.; Benitez, G.; Rubert, A. A.; Salvarezza, R. C. The Chemistry of the Sulfur-Gold Interface: In Search of a Unified Model. *Acc. Chem. Res.* **2012**, *45* (8), 1183−1192.
(56) Gruenwald, M.; Geissler, P. L. Patterns without Patches: Hierarchical Self-Assembly of Complex Structures from Simple Building Blocks. *ACS Nano* **2014**, *8* (6), 5891−5897.
(57) Chen, O.; Zhao, J.; Chauhan, V. P.; Cui, J.; Wong, C.; Harris, D. K.; Wei, H.; Han, H. S.; Fukumura, D.; Jain, R. K.; Bawendi, M. G. Compact High-Quality CdSe-CdS Core-Shell Nanocrystals with Narrow Emission Linewidths and Suppressed Blinking. *Nat. Mater.* **2013**, *12* (5), 445−451.
(58) Mokari, T.; Sztrum, C. G.; Salant, A.; Rabani, E.; Banin, U. Formation of Asymmetric One-Sided Metal-Tipped Semiconductor Nanocrystal Dots and Rods. *Nat. Mater.* **2005**, *4* (11), 855−863.

DOI: 10.1021/jacs.9b01033
J. Am. Chem. Soc. 2019, 141, 6013−6021